Use of heterogeneous background error covariance matrices at mesoscale

by Thibaut Montmerle *and Loïk Berre
Météo-France/CNRM-GAME, Toulouse, France

Summary

This study focuses on the feasibility of a simultaneous use of different background error covariance matrices at convective scale to make better use of observations linked to precipitation. Multivariate background error covariances have been computed separately for clear air and precipitating columns from an ensemble of AROME forecasts at 2.5 km horizontal resolution. Convection and microphysical processes, which are explicitly resolved, explain in particular the large discrepancies in correlation lengths, error variances and in the coupling between humidity, temperature and divergence errors. Theses results argue in favor of including an heterogeneous background error covariance matrix in AROME incremental 3Dvar. This can be achieved by expressing the analysis increment as the sum of two terms, one for precipitating areas and the other for non-precipitating areas, making use of a grid-point mask. This implies to double the size of the control variable and of the gradient of the cost function. The feasability of this method is shown through single observation experiments.

1 Introduction

The AROME NWP system runs operationally since December 2008 at Météo-France, providing forecast of potentially dangerous meteorological events and of lower tropospheric phenomena at convective scale. This system makes use of cycled assimilation/forecast steps based on a specific 3h Rapid Update Cycles (RUC) configuration (Brousseau *et al.*, 2008). AROME 3DVar uses a climatological multivariate background error covariance matrix (so-called **B** matrix) deduced from an ensemble-based method. As pointed out by Bannister (2008a) , **B** has a profound impact on the analysis, by i) weighting the importance of the a priori state, ii) smoothing and spreading information from observation points, iii) imposing balance between the model control variables. As a consequence, climatological covariances often produce unrealistic increment structures in regions characterized by strong gradients (precipitating fronts, top of boundary layer...), the information that is brought by observations spreading too much towards data sparse areas. Spatial localization and flow-dependency of background error covariances are thus required in order to get increments more adequately balanced and structured in regions characterized by different meteorological behaviors.

By using masks on forecast differences, section 2 presents to which extent modelled covariances can differ in clear air and in precipitating areas. The strongly different behaviors that have been found have lead us to develop an original method allowing to use different background error covariances in those regions. The theoretical aspects of such method, followed by a simple one-observation experiment, are discussed in section 3.

---

*corresponding author's address: thibaut.montmerle@meteo.fr

2 Background error covariance matrices for clear air and precipitating areas

2.1 Computation using an AROME ensemble at mesoscale

Berre (2000) has proposed a multivariate formalism for ALADIN adapted from Parrish *et al.* (1997) and Derber and Bouttier (1999) for global Numerical Weather Prediction (NWP) systems. This formalism uses linear balance relationships between errors of different physical quantities, computed from statistical regressions, with an extra balance relation for specific humidity. The use of spectral regressions allows us to obtain scale-dependent balance relationships that are representative of the area of interest, which is well suited for assimilation purposes at the mesoscale in any domain. The statistical relations read:

$$
\begin{aligned}
\zeta &= \zeta \\
\eta &= \mathcal{M}\mathcal{H}\zeta + \eta_u \\
(T, P_s) &= \mathcal{N}\mathcal{H}\zeta + \mathcal{P}\eta_u + (T, P_s)_u \\
q &= \mathcal{Q}\mathcal{H}\zeta + \mathcal{R}\eta_u + \mathcal{S}(T, P_s)_u + q_u
\end{aligned}
\tag{1}
$$

where $(\zeta, \eta, (T, P_s), q)$ are respectively forecast errors of vorticity, divergence, temperature and surface pressure, and specific humidity, which are the model control variables that are analyzed on model vertical levels; the subscript u stands for unbalanced (total minus balanced) fields. $\mathcal{M}, \mathcal{N}, \mathcal{P}, \mathcal{Q}, \mathcal{R}$ and $\mathcal{S}$ are vertical balance operators relating the spectral vertical profiles of predictors and those of the predictands. $\mathcal{H}$ is a horizontal balance operator that transforms the spectral coefficients of vorticity ζ into those of the balanced geopotential P_b (i.e $P_b = \mathcal{H}\zeta$). Balanced geopotential is supposed to be the balanced part of P_t, which is the linearized mass variable deduced from (T, P_s) by the linearized hydrostatic relationship.

Background error covariances are computed from two 6-member ensembles built with the ALADIN and AROME models at 10 km and 2.5 km horizontal resolution respectively, in cascade from the real time ARPEGE ensemble assimilation that runs operationally at Météo-France since July 2008 (Desroziers *et al.*, 2008). Each member has been computed for 17 precipitating cases chosen from April to July 2008. The ALADIN ensemble includes a perturbed 3DVar step (with perturbed backgrounds and observations), while the AROME ensemble has been conducted in spin-up mode, using the ALADIN ensemble as initial and coupling files. The AROME RUC (Rapid Update Cycle) being based on cycled assimilation/forecast steps every 3 hours (Brousseau *et al.*, 2008), statistics on 3h forecast differences $\varepsilon_b^{kl} = x_b^k - x_b^l$ between members (k, l) have been calculated.

However in this study, contrarily to the operational background error matrix, statistics have been computed separately for precipitating and for clear air areas using forecasts valid at 21 UTC, which corresponds approximately to the maximum of convective activity for the chosen dates. For that purpose, two masks have been built in order to take into account, in each pair of forecast, only profiles whose vertically integrated mixing ratios of precipitating rain do and do not exceed 0.1 $g.kg^{-1}$ respectively. The forecast difference field ε_b^{kl} is thus decomposed in three different terms:

$$
\varepsilon_b^{kl} \approx \left[G\delta_{p,p}^{kl}\right]\varepsilon_b^{kl} + \left[G\delta_{np,np}^{kl}\right]\varepsilon_b^{kl} + \left[G\delta_{p,np}^{kl}\right]\varepsilon_b^{kl}
$$

where $\delta_{p,p}^{kl}$ $(\delta_{np,np}^{kl})$ is a Kronecker-like operators equal to 1 in common precipitating (non-precipitating) areas between the two compared members (k, l), and equal to 0 elsewhere. In a similar way, $\delta_{p,np}^{kl}$ is equal to 1 in non-common areas. In order to smoothen the spatial structures

of these different terms, a gaussian blur G , based on a convolution with a 5x5 kernel, has been applied in addition to these operators.

2.2   Comparisons of statistics obtained for clear air and precipitating regions

2.2.1   Auto-covariances

Figure 1 shows the spectrally averaged vertical profiles of standard deviations of the forecast errors σ_b, as used in the AROME operational suite, and as deduced from the ensemble of precipitating cases. Note that standard deviations are rescaled with respect to their spatial sample size in cases where subdomains have been considered for their computation.
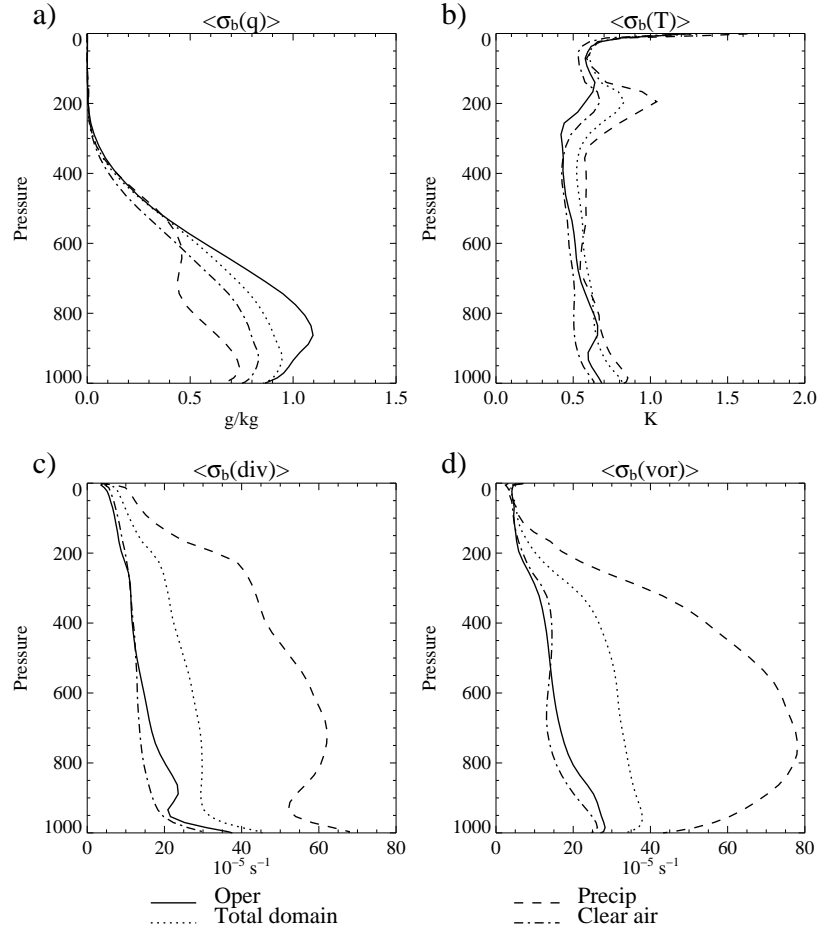
Figure 1:   Vertical profiles of mean standard deviation of (a) humidity, (b) temperature and surface pressure, (c) divergence and (d) vorticity forecast errors for AROME over France for the operational version (full line), and deduced from an ensemble of precipitating cases: total domain (dotted line), precipitating (dashed line) and non-precipitating areas (dotted-dashed line).

Smaller values are displayed for q and T over rainy areas, which is explained by the fact that, in this case, only saturated profiles characterized by small dispersion of q and T have been considered in the computation. Two maxima are displayed in the boundary layer and around 600 hPa, denoting variations of the level of free convection and of the cloud top. For this subdomain, values are also much larger at all altitudes for errors of ζ and η, reflecting the important small scale dynamical circulation within precipitating clouds. Variability in the low level convergence

and in the vertical extension of the clouds are in particular shown by the η profile. Statistics obtained by considering only clear air profiles are close to what is used operationally.

To compare horizontal correlations, horizontal length-scales as defined by Daley (1991) have been computed and the results are plotted in Fig. 2. Two times smaller lengthscales (5 vs 10 km approximately) are obtained over rainy areas compare to clear air for q and T. Furthermore for these variables, quasi-invariant values are displayed all over the vertical, contrarily to what is used in AROME operationnally, where lengthscales are increasing with height. This is probably due to the "verticality"of the bi-dimentional mask which is applied at all vertical levels. For ζ and η however, very similar profiles are obtained (not shown). These results indicated that much more localized increments can be obtained in precipitating areas using specific background error covariances. This is of great interest for high density observation networks like radar data or satellite radiances, since the representative scales of the resulting analyses should become much smaller (obviously by also paying attention to correlations between observation errors) and therefore more realistic.
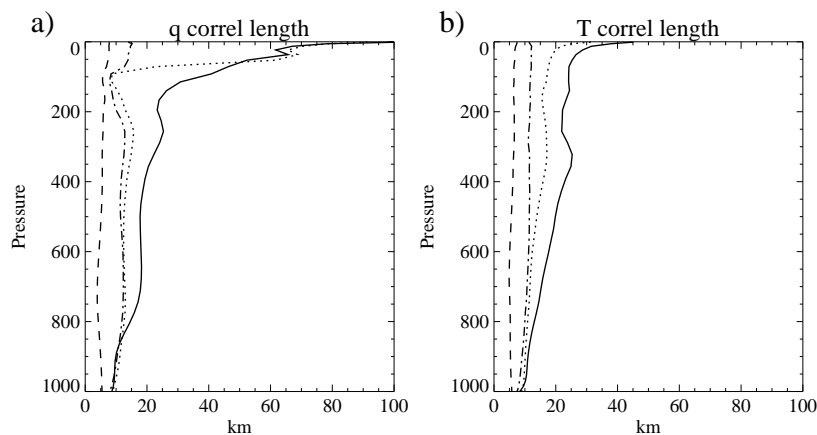
Figure 2: Vertical profiles of horizontal lengthscales (in km) of (a) humidity and (b) temperature forecast errors for AROME over France for the operational version (full line), and deduced from an ensemble of precipitating cases: total domain (dotted line), precipitating (dashed line) and non-precipitating areas (dotted-dashed line).

Signatures of vertical cloud development can be seen mainly on the mean vertical auto-correlations for q errors (and in a less extent for T and ζ) in the mid-troposphere for precipitating areas (not shown). This point denotes stronger vertical mixing within clouds performed by the explicitely resolved convection.

2.2.2   Cross-covariances

Variance ratios are used to compute the relative importance of the balanced and unbalanced terms following the multivariate approach defined in Eq. (1). They are given by the ratio of the variance of each balanced term divided by the total variance of the full field. They indicate the amount of increment for a given variable that will be balanced with increments of other variables.

Fig. 3 shows the vertical distribution of these ratios obtained over rainy and clear air areas for the specific humidity q field. The differences of behaviours between these two areas are striking: in clear air, the total explained variance of q is approximately 10% less balanced and is mainly controlled by the unbalanced mass field $(T, P_s)_u$ up to 400 hPa. On the opposite, the coupling with the unbalanced divergence η_u is much more important in rainy regions up to the

tropopause (Fig. 3.a) and for scales smaller than 100 km (not shown). For these latter regions, a maximum of variance around 800 hPa is explained mostly by η_u but also by $(T, P_s)_u$, and seems to correspond to the level of free convection with a maximum amplitude of convergence and of heating due to diabatic processes. In these precipitating regions, the coupling with balanced geopotential P_b is almost non-existent.
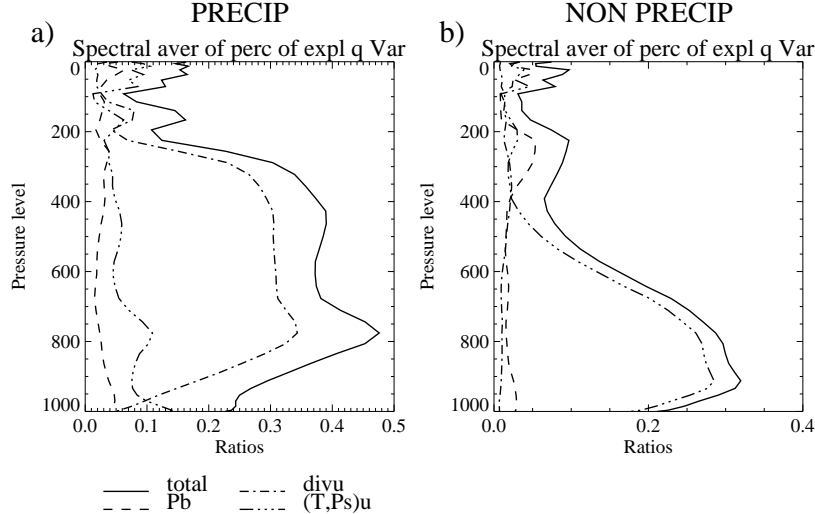
Figure 3: Spectral averages of the percentages of explained specific humidity q error variances as a function of height for AROME, computed over precipitating (left panels) and non-precipitating areas (right panels). P_b stands for the so-called balanced mass and divu for the unbalanced divergence (see text for details).

For rainy and clear air areas, the main predictors for the computation of the specific humidity forecast error covariances are thus respectively the unbalanced divergence η_u and the unbalanced temperature and surface pressure $(T, P_s)_u$. For rainy areas, spectrally averaged covariances between q and the total divergence η is coherent with the supply of humidity in convergent system: a positive increment of humidity at 800 hPa will result of a strong convergence below and divergence above (not shown). On the contrary, such a humidification has almost no impact on wind field in clear air conditions, appart from a weak local divergence. Intermediate behaviour is found for the operational background error covariances, which indicates that, in this case, increments are often balanced in a suboptimal way, either in precipitating (where the $q - \eta$ coupling is too weak) or in non-precipitating areas (where the $q - \eta$ coupling is too strong).

The strongly different behaviors that have been shown in this section, which are directely linked to convection processes that are resolved explicitly in AROME, confirm the interest of using simultaneously different statistics in regions with different meteorological patterns. Such a method would indeed allow increments to be more adequately balanced and structured in those regions, and thus to make better use of observations in a data assimilation system.

3   Implementation of a heterogeneous B matrix in a 3DVAR

3.1   Theoretical aspects

Following an initial idea by Courtier *et al.* (1998) , we propose here to express the **B** matrix as a linear combination of two terms, each term characterizing non precipitating (np subscript) and precipitating (p subscript) areas respectively:

$$\mathbf{B} = \alpha^{1/2} \mathbf{B_{np}} \alpha^{\mathbf{T}/2} + \beta^{1/2} \mathbf{B_p} \beta^{\mathbf{T}/2} \tag{2}$$

which can also be expressed as:

$$\mathbf{B} = \mathbf{B^{1/2}}\mathbf{B^{T/2}} = \left(\begin{array}{cc} \alpha^{1/2}\mathbf{B_{np}^{1/2}} & \beta^{1/2}\mathbf{B_p^{1/2}} \end{array} \right) \left(\begin{array}{c} \mathbf{B_{np}^{T/2}}\alpha^{T/2} \\ \mathbf{B_p^{T/2}}\beta^{T/2} \end{array} \right) \tag{3}$$

α and β define the areas where the non-precipitating and the precipitating statistics are applied respectively. These operators are based on 2D grid point masks that could be deduced from radar observations. The elliptic truncation used in ALADIN (Radnóti and et al., 1996), and consequently AROME, ensures a smooth transition of increment structures between areas that use different statistics, thanks to the final use of Fourier transform in these operators. Theoretically, other terms could be added to this expression, each of these additional terms being applied exclusively to another part of the domain where the analysis is performed. One can imagine for example partitioning precipitating areas into convective and stratiform parts, or clear air areas into stable and unstable parts.

AROME 3DVar uses an incremental formulation (Courtier *et al.*, 1994), where the increment δx is written as the control variable χ renormalized by $\mathbf{B^{1/2}}$:

$$\delta x = \mathbf{B^{1/2}}\chi$$

Considering eq.(3), the increment writes as a linear combination of two terms:

$$\delta x = \alpha^{1/2}\mathbf{B_{np}^{1/2}}\chi_1 + \beta^{1/2}\mathbf{B_p^{1/2}}\chi_2 \tag{4}$$

Thus, this method implies in particular to double the size of the control vector. In the space of this renormalized control variable, the J^b cost function and its gradient become trivial:

$$J_\chi^b = \frac{1}{2}\chi^T\chi = \frac{1}{2}\left(\begin{array}{cc} \chi_1 & \chi_2 \end{array} \right)^T \left(\begin{array}{c} \chi_1 \\ \chi_2 \end{array} \right) \tag{5}$$

$$\nabla_\chi J^b = \chi = \left(\begin{array}{c} \chi_1 \\ \chi_2 \end{array} \right) \tag{6}$$

In the same space, the J^o cost function and its gradient write:

$$J_\chi^o = \frac{1}{2}\left(\mathbf{H}(\alpha^{1/2}\mathbf{B_{np}^{1/2}}\chi_1 + \beta^{1/2}\mathbf{B_p^{1/2}}\chi_2) - \mathbf{d} \right)^T \mathbf{R^{-1}}\left(\mathbf{H}(\alpha^{1/2}\mathbf{B_{np}^{1/2}}\chi_1 + \beta^{1/2}\mathbf{B_p^{1/2}}\chi_2) - \mathbf{d} \right) \tag{7}$$

$$\nabla_\chi J^o = \left(\begin{array}{c} \mathbf{B_{np}^{T/2}}\alpha^{T/2} \\ \mathbf{B_p^{T/2}}\beta^{T/2} \end{array} \right) \mathbf{H^T}\mathbf{R^{-1}}\left(\mathbf{H}(\alpha^{1/2}\mathbf{B_{np}^{1/2}}\chi_1 + \beta^{1/2}\mathbf{B_p^{1/2}}\chi_2) - \mathbf{d} \right) \tag{8}$$

As for the control variable, the size of the gradient of the cost function must then also be doubled (or multiplied by the number of different $\mathbf{B}$ matrices used in eq.(3), if more than 2 matrices are used).

4 Results of single observation experiments

To ensure the reliability of the new formulation of the variational system described in the previous section, three different experiments have been performed:

- **CNTRL-Bnp** aims at controlling the impact on analysis of the non-precipitating $\mathbf{B}_{np}$ matrix, using the standard formulation of the variational system (e.g. considering only one $\mathbf{B}$ matrix). For that purpose, four pseudo-observations, whose localizations are 48N/4.5E and 42.5N/4.5E at 800 and 500 hPa, are assimilated. These pseudo-observations have been generated by considering -30% relative humidity innovations (e.g. observation minus background) at those locations.

- **CNTRL-Bp** is the equivalent of CNTRL-Bnp but using the precipitating $\mathbf{B}_p$ matrix.

- **Bnp-Bp** uses the hybrid formulation of eq.3 and other ingredients listed in the previous section in the variational system, considering that the northern (e.g. North of 46.5N) and the southern halfs of the domain as precipitating and non-precipitating areas respectively.

(a) Non-Precipitating area

(b) Precipitating area

(c) Mixed
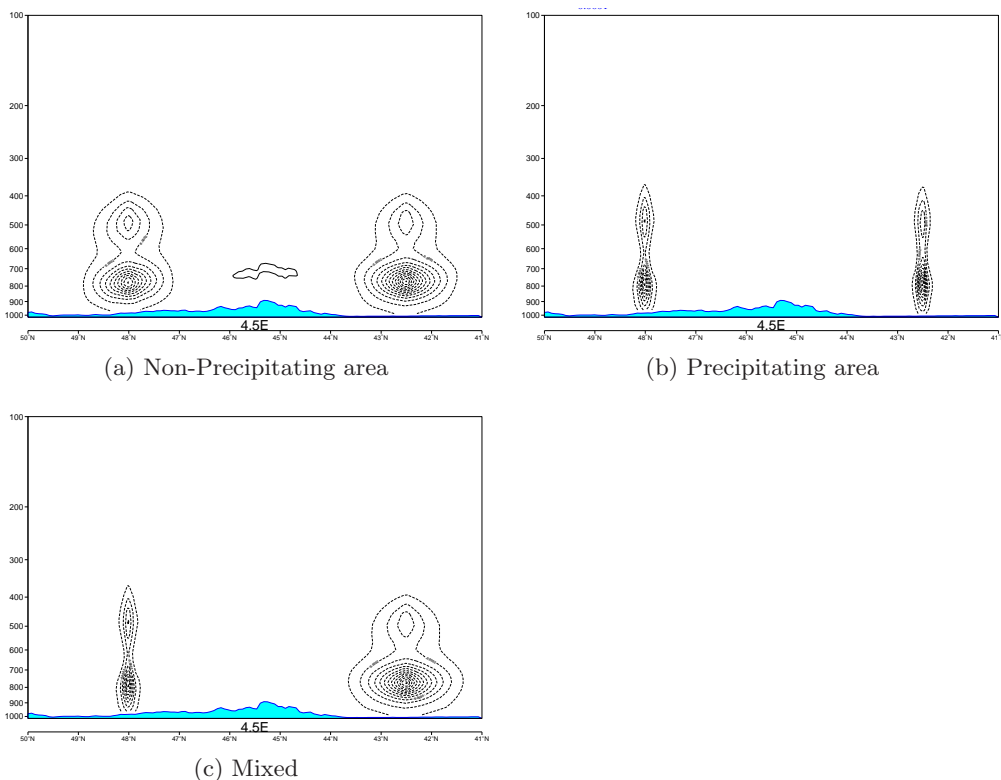
Figure 4:   Vertical north-south cross-sections of specific humidity increments (isocontours 0.1 g/kg) for (a) the CNTRL-Bnp, (b) the CNTRL-Bp and (c) the Bnp-Bp experiments (cf. text for details)

The large differences of correlation lengths between the two $\mathbf{B}$ matrices displayed in Fig.2 directly impact the structure of the increments, much tighter increments being obtained in CNTRL-Bp than for CNTRL-Bnp (Figs. 4.b and 4.a respectively). Some differences in the vertical structures can be identified too, especially near the boundary layer. Increments of temperature differ also quite significantly due to changes in the balances (not shown). The Bnp-Bp experiment displays what was expected: in the "rainy"northern part and in the "non-precipitating"southern part of the domain , Fig.4.c shows exactly the same increment structures

as CNTRL-Bp and as CNTRL-Bnp respectively. This is a proof of concept, that increments with very different behaviours, in terms of intensities and shapes, can be obtained simultaneously using the heterogeneous **B** matrix formulation, and that different balance relationships can be used over different areas in a more adapted way.

5   Conclusion

Using ensemble information at convective scale with AROME, it has been shown that background error covariances strongly differ in clear air and in precipitating areas, and that these differences are coherent with explicit convection processes. Precipitating regions are particularly characterized by shorter correlation lengths, larger background error standard deviations for small scale dynamical variables, larger vertical correlations for the specific humidity in the mid-troposphere, very different balance relationships between the specific humidity and the unbalanced divergence. An original method has then been developped in order to use simultaneously these different backgound error covariances in VAR, allowing to make better use of observations through the better localization of increments and the more adequate balance relationships. This method is currently tested on real cases by considering radar reflectivities in AROME data assimilation system.

References

Berre, L. (2000). Estimation of synoptic and mesoscale forecast error cavariances in a limited area model. *Mon. Wea. Rev. 128*, 644–667.

Brousseau, P., F. Bouttier, G. Hello, Y. Seity, C. Fischer, L. Berre, T. Montmerle, L. Auger, and S. Malardel (2008). A prototype convective-scale data assimilation system for operation : the Arome-RUC. *HIRLAM Techn. Report 68*, 23–30.

Courtier, P., E. Andersson, W. Heckley, J. Pailleux, D. Vasiljevic, , A. Hollingsworth, M. Fisher, and F. Rabier (1998). The ecmwf implementation of three-dimensional variational assimilation (3d-var). i: Formulation. *124*, 1783?1807.

Courtier, P., J.-N. Thépaut, and A. Hollingsworth (1994). A strategy for operational implementation of 4d-var using an incremental approach. *120*, 1367–1387.

Daley, R. (1991). Atmospheric data analysis. Cambridge University Press, pp. 460.

Derber, J. and F. Bouttier (1999). A reformulation of the background error covariance in the ECMWF global data assimilation system. *Tellus 51A*, 195–221.

Desroziers, G., L. Berre, O. Pannekoucke, S. Stefanescu, P. Brousseau, L. Auger, B. Chapnik, and L. Raynaud (2008). Flow-dependent error covariances from variational assimilation ensembles on global and regional domains. *HIRLAM Techn. Report 68*, 5–22.

Parrish, D., J. Derber, R. Purser, W.-S. Wu, and Z.-X. Pu (1997). The NCEP global analysis system: recent improvements and future plans. *75*, 359–365.

Radnóti, G. and et al. (1996). The spectral limited area model ARPEGE-ALADIN. In *PW-PRR Report*, Volume n.7, pp. 111–118. World Met. Org.